MATERIALS SCIENCE

Carbon-free high-performance cathode for solid-state Li-O₂ battery

Mokwon Kim[1], Hyunpyo Lee[1], Hyuk Jae Kwon[1], Seong-Min Bak[2], Cherno Jaye[3], Daniel A. Fischer[3], Gabin Yoon[1], Jung O. Park[1], Dong-Hwa Seo[4], Sang Bok Ma[1]*, Dongmin Im[1]

The development of a cathode for solid-state lithium-oxygen batteries has been hindered in practice by a low capacity and limited cycle life despite their potential for high energy density. Here, a previously unexplored strategy is proposed wherein the cathode delivers a specific capacity of 200 milliampere hour per gram over 665 discharge/charge cycles, while existing cathodes achieve only ~50 milliampere hour per gram and ~100 cycles. A highly conductive ruthenium-based composite is designed as a carbon-free cathode by first-principles calculations to avoid the degradation associated with carbonaceous materials, implying an improvement in stability during the electrochemical cycling. In addition, water vapor is added into the main oxygen gas as an additive to change the discharge product from growth-restricted lithium peroxide to easily grown lithium hydroxide, resulting in a notable increase in capacity. Thus, the proposed strategy is effective for developing reversible solid-state lithium-oxygen batteries with high energy density.

INTRODUCTION

Li-O₂ batteries are promising candidates as next-generation energy storage systems, because their theoretical specific energy (~3458 Wh/kg) is much higher than that of current Li-ion batteries (1–6). However, the currently available aprotic Li-O₂ batteries typically show limited cyclability because of the decomposition of the organic electrolytes by the highly oxidative radicals formed at the cathode (7–14). To solve this problem, solid-state cathodes composed of stable ceramic electrolytes instead of organic ones have been developed recently (15–18). In general, these cathodes provide a capacity, as they result in the formation of Li₂O₂ as the discharge product through an electrochemical reaction among the Li⁺ ions, electrons, and O₂ gas. However, the growth of Li₂O₂ particles within the solid-state cathode is limited (<50 nm in thickness) because of the poor electron/ion transport in Li₂O₂ and the absence of a liquid medium for Li₂O₂ growth (19, 20). Therefore, the capacity of Li₂O₂-based Li-O₂ batteries with a solid-state cathode is inevitably limited. One way to overcome the capacity limitation resulting from the restricted growth of Li₂O₂ particles within the solid-state cathode is to provide conditions conducive to the growth of the discharge product. It is known that LiOH can grow via strong O_2^- intermediate solvation by water with a high acceptor number in a water-containing environment (21–28). Thus, the addition of water vapor to the O₂ gas used in solid-state batteries could effectively provide water to the cathode to change the discharge product from growth-restricted Li₂O₂ to easily grown LiOH, as depicted in Fig. 1. It can be speculated that the water vapor would play three important roles on the performance of Li-O₂ battery. The first role of the water vapor is to increase the capacity. Because a larger amount of the growable discharge product (LiOH) could be accommodated on the surface of

the cathode and within its pores, a capacity higher than that of conventional Li₂O₂-based batteries could be achieved. The second is to raise the discharge voltage. The water vapor could induce the electrochemical formation of LiOH at 3.4 V (versus Li/Li⁺), while Li₂O₂ was formed at 2.96 V in the absence of water vapor. The third is to enhance the kinetics. The discharge product of LiOH could act as a Li⁺ ion conductor in the solid-state cathode when it is hydrated, implying an improvement in rate capability. Therefore, it is expected that a remarkable enhancement in energy density of solid-state Li-O₂ batteries would be achieved by the water vapor addition. In addition, the decomposable carbonaceous materials are completely excluded from the cathode, which can improve long-term cycling stability of the cell.

In this study, we first report an effective strategy to simultaneously improve the capacity and reversibility of the solid-state Li-O₂ battery by introducing the carbon-free ceramic cathode material and LiOH-based reaction chemistry. A both electronic and ionic conducting ruthenium-based composite (RBC) was designed as a solid-state cathode to eliminate the parasitic chemistry of conducting carbons. In addition, LiOH-based reaction chemistry was induced by the addition of water vapor to deliver a high capacity. The formation and growth of LiOH as a discharge product via the water vapor–assisted cathode reaction were confirmed through electrochemical and structural analyses of the cathode, including O K-edge x-ray absorption near-edge structure (XANES) measurements. A solid-state Li-O₂ cell with an RBC cathode in humidified O₂ with 4 weight % (wt %) water vapor showed a specific capacity of 200 mA·hour/g_cathode (gram based on the total weight of the RBC cathode) over 665 discharge-charge cycles. This approach provides novel insights into the development of efficient ceramic-based solid-state cathodes for practical Li-O₂ battery.

RESULTS AND DISCUSSION

Design and synthesis of RBC material

An RBC containing Ru(IV) ions was developed for use as a cathode material for solid-state Li-O₂ batteries by combining RuO₂ (electron-conducting catalyst) and La₂LiRuO₆₋δ (Li-containing catalyst) owing to the high conductivities and electrocatalytic activities of these

[1]Battery Material Lab, Samsung Advanced Institute of Technology, Samsung Electronics, Suwon, Gyeonggi-do 16678, Republic of Korea. [2]National Synchrotron Light Source II, Brookhaven National Laboratory, Upton, NY 11973, USA. [3]Material Measurement Laboratory, National Institute of Standards and Technology, Gaithersburg, MD 20899, USA. [4]Department of Energy Engineering, School of Energy and Chemical Engineering, Ulsan National Institute of Science and Technology (UNIST), Ulsan 44919, Republic of Korea.
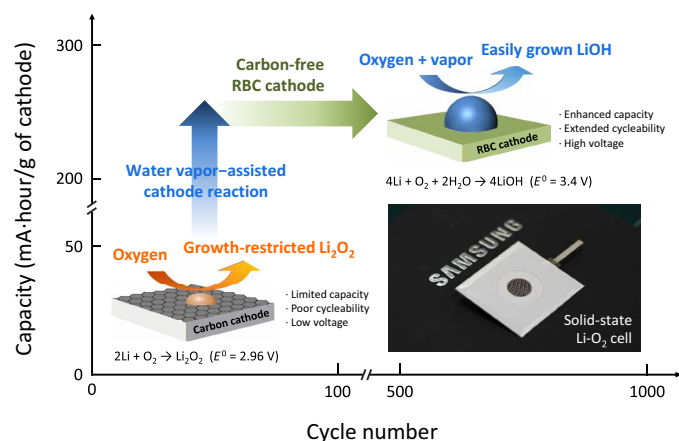*Corresponding author. Email: sangbok.ma@samsung.com

Fig. 1. Schematic illustration of proposed solid-state Li-O$_2$ battery. Discharge behavior of solid-state Li-O$_2$ cell with RBC cathode during operation in dry and humidified O$_2$ atmosphere with added water vapor.

components for LiOH-based reaction chemistries. RuO$_2$ is a known electronic conductor with a narrow bandgap (Fig. 2A) and is a catalyst for oxygen redox reactions (29–32). The perovskite La$_2$LiRu(IV)O$_{6-\delta}$ also has narrow bandgap (Fig. 2B), implying high electronic conductivity, which is mainly attributed to the reduced Ru ions with the oxygen vacancy (fig. S1, A and B). In addition, the Ru ions in the perovskite can act as catalytic centers for the oxygen redox reaction (33, 34). As shown in Fig. 2C, on the basis of Rietveld refinement, the x-ray diffraction (XRD) peaks of the synthesized RBC were indexed to a tetragonal RuO$_2$ structure (space group: $P4_2/mnm$, $a = b = 4.493$ and $c = 3.106$ Å) (35) and a monoclinic perovskite La$_2$LiRuO$_6$ structure (space group: $P2_1/c$, $a = 5.554$, $b = 5.620$, $c = 9.618$ Å, and $\beta = 125.25°$) (36). These results confirmed that the RBC was synthesized successfully. To evaluate the oxidation state of Ru in the RBC, we measured the normalized Ru K-edge XANES spectra (Fig. 2D). The main absorption edge energy for the purely dipole-allowed 1s→5p transition (37) was similar for RBC and RuO$_2$, indicating that they had the same average oxidation state of +4.0. This implies that La$_2$LiRuO$_{6-\delta}$ in RBC also consists of Ru(IV) ions. This result is consistent with the design strategy for developing an RBC containing Ru(IV) ions to increase the conductivity.

Morphological and elemental analyses of the RBC nanoparticles were performed using high-angle annular dark-field scanning transmission electron microscopy (HAADF-STEM), as shown in Fig. 2E. The primary particle size of the RBC is approximately 20 to 100 nm, and the agglomerated particle became about 100 to 300 nm in size. The surface area by the Brunauer-Emmett-Teller analysis was 10.2 m^2/g. The elemental maps for the RBC nanoparticles showed that Ru atoms were distributed homogeneously within both RuO$_2$ and La$_2$LiRuO$_{6-\delta}$ nanocrystals in the expected atomic ratios (table S1). The uniform distribution of Ru atoms could enhance the catalytic effect in a Li-O$_2$ battery. The electronic and Li$^+$-ion conductivities of the RBC were measured by the dc method using ion- and electron-blocking cells, respectively (38–39). The measured electronic and Li$^+$-ion conductivities of the RBC pellets were 2.4×10^{-3} and 5.1×10^{-6} S/cm, respectively (fig. S2). These values are reasonable and indicated that the RBC is suitable for use as a substrate for the formation of the discharge product in Li-O$_2$ batteries. The electrochemical stability of the RBC was also investigated

through cyclic voltammetry (CV) in an organic electrolyte, 1 M lithium bis(trifluoromethylsulfonyl)imide in propylene carbonate (LiTFSI in PC), as shown in Fig. 2F. No distinct redox current peak was observed in the CV curve, implying that the RBC was electrochemically stable within the voltage window of 2.2 to 4.5 V (versus Li/Li$^+$). This is consistent with the CV result of the solid-state Li-O$_2$ cell using the RBC cathode in Ar atmosphere, which showed only the current from the Ti^{4+}/Ti^{3+} redox in LATP (Li$_{1+x+y}$Al$_x$Ti$_{2-x}$Si$_y$P$_{3-y}$O$_{12}$) was observed under ~2.5 V (fig. S3). Thus, on the basis of the observed conductivity and stability of the RBC, it was concluded that it is suitable for use as a cathode material.

Water vapor–assisted cathode reaction

A Li-O$_2$ cell (~3 cm by 3 cm) with an RBC cathode was fabricated using a pouch-type Li-protective anode to protect the Li metal from moisture, as depicted in fig. S4. The porous RBC cathode layer (thickness of $t = 2$ μm and diameter of $d = 8$ mm) on a ceramic electrolyte layer (LATP; $t = 250$ μm, 2.5 cm by 2.5 cm; OHARA Inc.) was prepared by the sintering process at 400°C with a porosity of ~40% to provide the gas diffusion path and to accommodate the discharge product (fig. S5). The RBC cathode–attached LATP layer, the electrolyte (1 M LiTFSI in PC) with a polymer separator ($t = 25$ μm, 2.8 cm by 2.8 cm) as an interlayer, and a piece of Li metal foil ($t = 175$ μm, 2.4 cm by 2.4 cm) were vacuum-sealed using thermoplastic sealing film while leaving a 16-mm-diameter window. The cell was tested in a humidified O$_2$ generated by adding 4 wt % water vapor to pure O$_2$ gas. To elucidate the effect of the added water vapor, we performed CV measurements with the cathode in an O$_2$ atmosphere with/without water vapor for voltages of 2.2 to 4.5 V (versus Li/Li$^+$) at 40°C with a scan rate of 0.5 mV/s. As shown in Fig. 3A, no redox feature was observed in dry O$_2$, because the rate-controlling step for the reduction of O$_2$ (O$_2$ + e^- → O$_2^-$) was hindered by the high kinetics barrier of the solid-state cathode (40). The small reduction and oxidation peaks around ~2.5 and ~3.7 V were observed in the CV of the cell in dry O$_2$ at a lower scan rate of 0.05 mV/s at 60°C, which implies that the oxygen redox in the solid-state cathode could hardly occur at the solid-gas interphase (fig. S6). In contrast, distinct redox peaks were observed at approximately 3.0 V (reduction) and 3.5 V (oxidation) in humidified O$_2$, indicating that the cathode reaction was activated within the cathode by the water vapor. The higher onset potential of ~3.4 V for reduction in humidified O$_2$ compared to that in dry O$_2$ at lower scan rate of 0.05 mV/s also supports that the discharge reaction was changed to a different reaction from the Li$_2$O$_2$ formation by the water vapor (fig. S7).

Figure 3B shows the typical discharge-charge profiles of the Li-O$_2$ cell at a constant current density of 10 mA/g$_{cathode}$. The profiles were measured in humidified O$_2$ at 40°C. The measured discharge voltage plateau (~3.0 V) in the presence of water vapor was higher than the practical voltage for Li$_2$O$_2$ formation ($E^0 = 2.96$ V versus Li/Li$^+$) in an aprotic Li-O$_2$ battery. This may be attributed to the H$_2$O-assisted oxygen reduction reaction producing LiOH ($E^0 = 3.4$ V versus Li/Li$^+$) as the discharge product. To clarify the effect of water vapor, the Li-O$_2$ cell using RBC cathode was discharged/charged in dry O$_2$ first and stopped after the charge and then discharged in humidified O$_2$ with 4 wt % water vapor. As shown in the fig. S8, the cell in dry O$_2$ was discharged with a voltage plateau of ~2.5 V for the formation of Li$_2$O$_2$. During charging, the charging voltage lastly reached to 4.5 V at the end of the charge. After adding
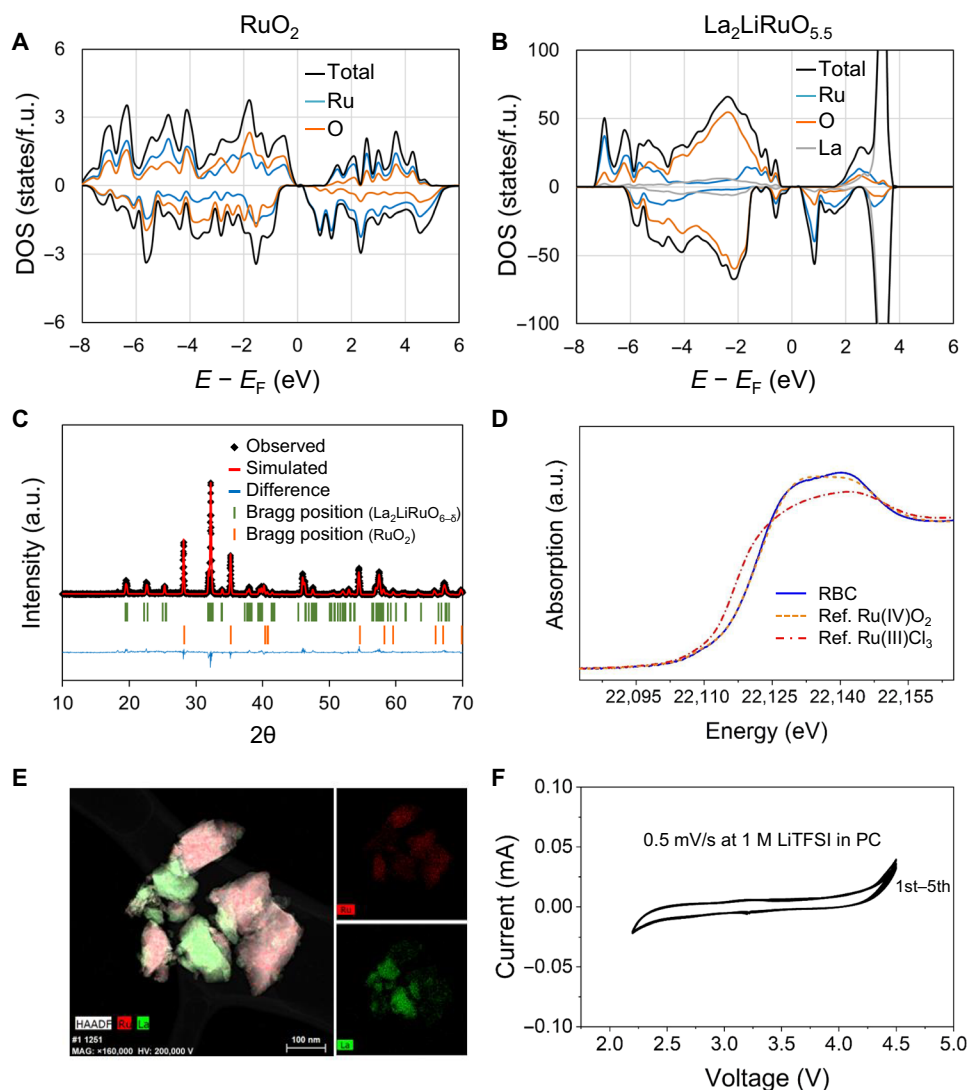
Fig. 2. Design of RBC cathode. Computed density of states (DOS) for (**A**) RuO_2 and (**B**) $La_2LiRuO_{5.5}$. f.u., formula unit. (**C**) Observed (dots) and simulated (lines) XRD patterns for synthesized RBC. Residuals and peak positions (|) appear below the data. a.u., arbitrary units. (**D**) Ru K-edge XANES spectra of RBC and reference oxides. (**E**) HAADF-STEM images and corresponding elemental maps for Ru and La. (**F**) CV profile of RBC cathode measured in 1 M LiTFSI in PC.

4 wt % water vapor, the cell was discharged at ~3.1 V, implying that the water vapor changed the primary reaction pathway to the direct electrochemical formation of LiOH instead of Li_2O_2. The higher discharge voltage in humidified O_2 was confirmed by the galvanostatic intermittent titration technique (GITT) during discharge of the Li-O_2 cell. For comparison, a Li-O_2 cell with a liquid organic electrolyte, 1 M LiTFSI in tetraethylene glycol dimethyl ether, which was free of water vapor, was also measured (Fig. 3C). The Li-O_2 cells were discharged at a constant current density of 10 mA/$g_{cathode}$ for 1 hour; this was followed by resting for 5 hours. The voltage of the relaxed cell with the liquid electrolyte was ~2.9 V and close to the typical voltage for Li_2O_2 formation in aprotic Li-O_2 batteries. The cell voltage increased to ~3.4 V for the Li-O_2 cell in humidified O_2, implying that the added water vapor changed the primary reaction pathway such that LiOH was the preferred discharge product instead of Li_2O_2. Moreover, despite being a solid-state cell, it showed a low overpotential of ~0.6 V during charging in humidified O_2 (Fig. 3B).

An increase in the discharge voltage and decrease in the charge voltage increases the energy efficiency of the cell. From the discharge-charge profile of the cell, its calculated energy efficiency was 81.4%, which is much higher than those reported previously for Li_2O_2-based solid-state Li-O_2 batteries free of water vapor (*15*–*17*). In addition, the Ru-based catalysis of the LiOH-based reaction chemistries at the RBC cathode, along with the presence of water, probably reduced the overpotential during discharge-charge of the cell.

In addition, the Li-O_2 cell containing water vapor had enhanced rate performance (Fig. 3D). During these measurements, the cell was discharged/charged at current densities of 10 to 100 mA/$g_{cathode}$, with a cutoff capacity of 100 mA·hour/$g_{cathode}$. In solid-state Li-O_2 batteries, charge transport is limited by the propagation of Li$^+$ ions through the discharge product, especially at the cathode-particle surfaces. Under humid conditions, the LiOH acts as a Li$^+$-ion conductor. This decreases the resistance to Li$^+$-ion conduction at the
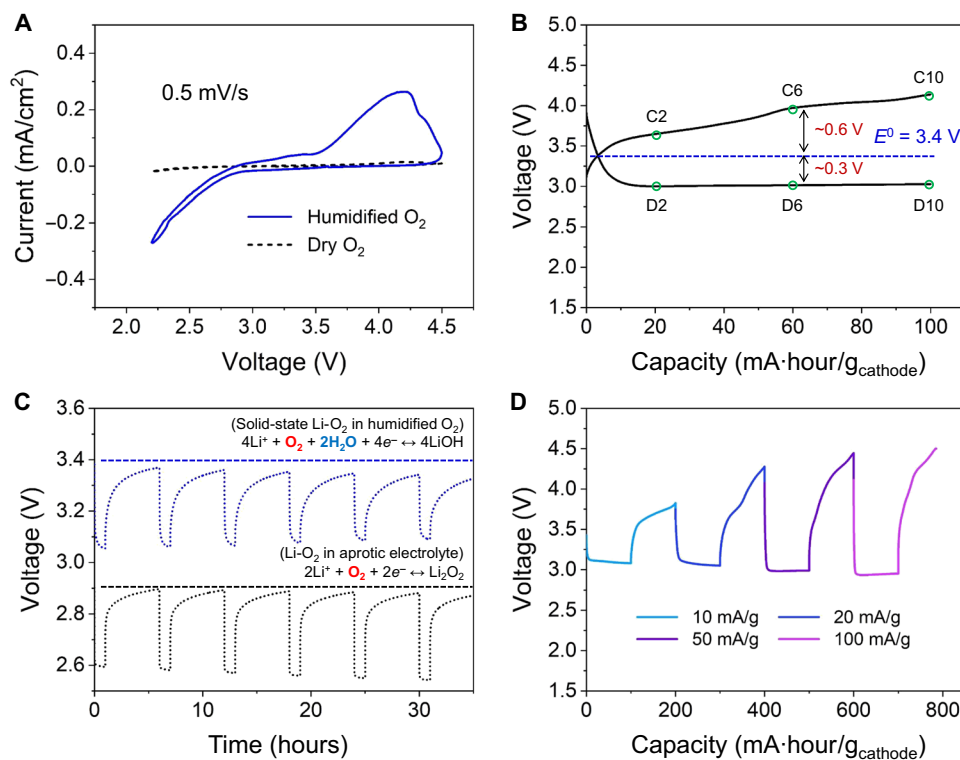
Fig. 3. Electrochemical characterizations of Li-O₂ cell with water vapor. (**A**) CV profiles of Li-O₂ cells with RBC cathode operated in dry O₂ without water vapor and humidified O₂ with 4 wt % water vapor. (**B**) Discharge-charge profiles of Li-O₂ cell in humidified O₂. (**C**) Comparison of galvanostatic intermittent titration technique (GITT) results to Li-O₂ cell tested in liquid electrolyte without water vapor. (**D**) Rate capability of Li-O₂ cell with RBC cathode in humidified O₂.

solid-solid interfaces between cathode particles, resulting in a higher rate capability of the cell. The enhanced electrochemical behavior of the Li-O₂ cell is attributed to improved reaction kinetics and an increase in the amount of reaction sites within the cathode in the presence of water vapor.

From the above results, it is concluded that the humidity plays three important roles on the performance of solid-state Li-O₂ battery. The first role of the humidity is to increase the capacity. The easily grown LiOH can be formed with the humidified O₂, while the growth-restricted Li₂O₂ is deposited in dry O₂. This is a meaningful advance for a solid-state Li-O₂ cathode, compared with a smaller discharge capacity in dry O₂. The second is to raise the discharge voltage. The water vapor can induce the electrochemical LiOH formation at 3.4 V. This is obviously higher than the Li₂O₂ formation voltage of 2.96 V. Thus, a positive change in energy density should be remarkable because of a voltage jump with a capacity increase by the water vapor addition. The third is to enhance the kinetics. Once the discharge product of LiOH can absorb the water vapor, it becomes a hydrated LiOH and acts as a Li⁺-ion conductor in the solid-state cathode.

Reversibility of the cathode reaction

Structural and compositional analyses of the cathode are essential for understanding its reaction chemistry during operation. The differential electrochemical mass spectrometry is known as an effective way to investigate the chargeability of LiOH in the Li-O₂ cells. The direct observation of the O₂ evolution during the charge of LiOH was reported in previous papers (*27, 28*). However, in case of

the humidified Li-O₂ cell, it is very difficult to measure the O₂ evolution due to the water contamination of the gas chromatography and mass spectrometry instruments. Instead, soft x-ray absorption spectroscopy (sXAS), scanning electron microscopy (SEM), and XRD analysis were selected, as they could also provide the intuitive information on the chargeability of LiOH.

When the amount of discharge product formed on the cathode is small, e.g., at the early stage of discharge, it is difficult to detect the discharge product from the spectroscopy owing to the high intensity of cathode and electrolyte materials. To investigate the water vapor–assisted cathode reaction, we performed sXAS due to its high elemental and chemical sensitivity. Figure 4A shows the partial electron yield (PEY) spectra as obtained from O K-edge XANES measurements of the cathodes prepared at different stages of the discharge-charge processes. The data correspond to the points shown in the discharge-charge profile in Fig. 3B. In the near-surface (5 to 10 nm) PEY spectra of the cathode, an absorption feature related to LiOH was observed even at point *D2* (after the cathode had been discharged for 2 hours at a current density of 10 mA/g₍cathode₎). This suggests that the cathode reaction of the Li-O₂ cell operated in humidified O₂ changed to a LiOH-based reaction in the presence of water. In contrast, when the cell was charged (C2 to C10) immediately after being discharged, the intensity of the absorption peak at ~533 eV decreased, and the peak eventually disappeared at the end of the charging process (C10), indicating the complete removal of LiOH from the cathode surface. The appearance and disappearance of peaks related to LiOH confirmed the reversible formation and decomposition of LiOH on the cathode.
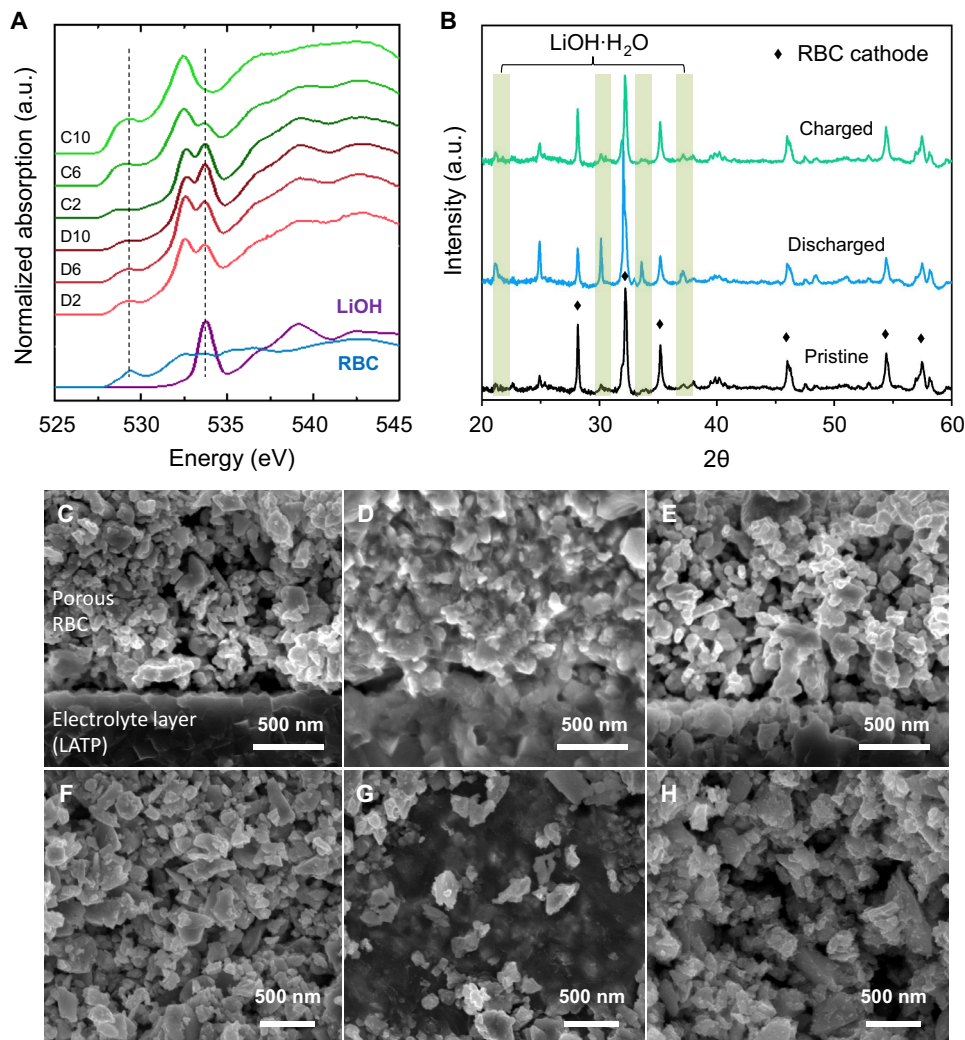
Fig. 4. Reversibility of cathode reaction in presence of water vapor. (**A**) PEY spectra from O K-edge XANES measurements of cathodes at different stages of the discharge/charge processes corresponding to the points shown in the discharge-charge profile in Fig. 3B. (**B**) XRD patterns and (**C** to **E**) top-view and (**F** to **H**) cross-sectional SEM images of pristine, discharged, and charged RBC cathodes after operation in humidified O_2.

Figure 4B shows XRD patterns of the cathode in different states (pristine, discharged, and recharged at an areal capacity of 1 mA·hour/ cm^2). In the discharged state, the cathode showed diffraction peaks at 2θ of 21.4°, 30.1°, 33.6°, and 36.9°. These were assigned to LiOH monohydrate (LiOH·H_2O), again confirming that LiOH was formed instead of Li_2O_2, which was converted to the hydrated form in the presence of water vapor. Furthermore, a Fourier transform infrared (FTIR) spectrum of the discharged cathode contained a sharp peak related to the —OH stretching mode at 3560 cm^{-1} (fig. S9). This peak was attributed to LiOH·H_2O, which shows broad absorbance at 2500 to 3200 cm^{-1} due to the hydrogen-bonded LiOH hydroxyl groups or the structural water molecules present within LiOH (*41*). On the basis of these results for the Li-O_2 cell in humidified O_2, it can be concluded that LiOH-based cathode reactions occurred, and the discharge product was evidently LiOH. After charging, the XRD peaks of LiOH·H_2O disappeared completely, indicating that the water vapor–assisted cathode reaction is highly reversible, even in an all–solid-state ceramic cathode without any organic components.

The morphology of the cathode in the pristine, discharged, and recharged states was also analyzed using SEM to determine the distribution of the discharge product and further confirm the high reversibility of the cathode reaction. The pristine cathode formed on an LATP layer had a porous morphology, which provided a large number of cavities for growth of the discharge product (Fig. 4C). During discharge (Fig. 4D and fig. S10), the discharge product of LiOH grew on the surfaces of the RBC nanoparticles and filled the cathode pores. The distribution of the discharge product in the cathode changed notably in the presence of water vapor. In dry O_2, the growth-restricted discharge product (mainly Li_2O_2) was formed only at the surface of the cathode structure (fig. S11), which is consistent with previous reports (*15, 17*). In contrast, when water vapor was introduced, the discharge product was formed in all cathode pores. After the subsequent recharging process, the discharge product disappeared, and empty pores were observed (Fig. 4E). The formation and decomposition of the discharge product in the humidified O_2 atmosphere was also confirmed by top-view SEM (Fig. 4, F to H).

Long-term cycling of Li-O₂ cell with water vapor

To evaluate the cycling performance of solid-state Li-O₂ cell with an RBC cathode, we cycled the cells with different discharge depths. The Li-O₂ cells showed highly reversible discharge/charge behaviors at different cutoff capacities of 100, 150, and 200 mA·hour/$g_{cathode}$ with a potential gap between discharge and charge of ~1.1 V, corresponding to energy efficiencies of 73.3, 72.5, and 72.6%, respectively (Fig. 5A). The long-term discharge-charge profiles of the cell with
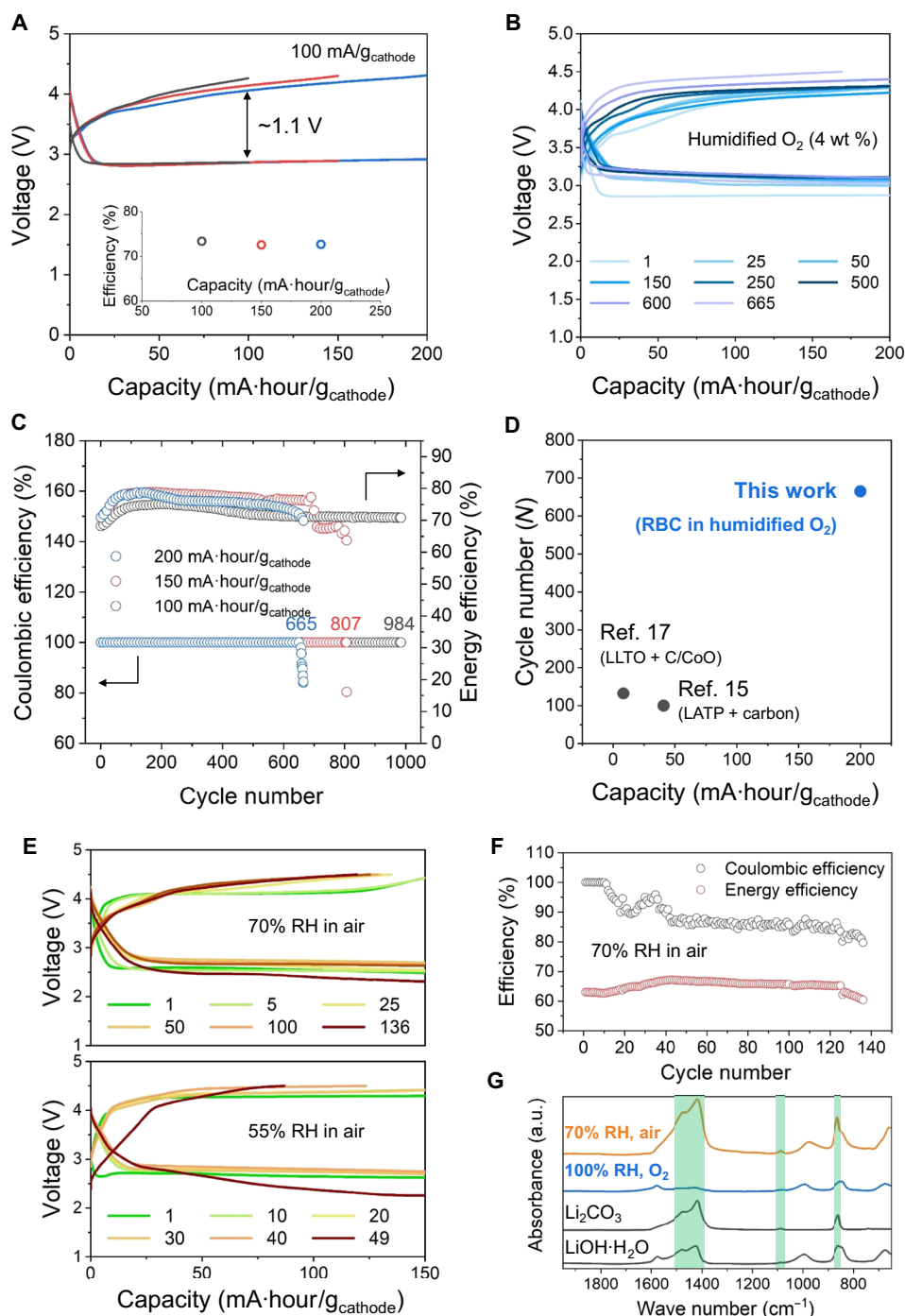
Fig. 5. Cycling performance of cell with water vapor. (**A**) Typical discharge-charge profiles of solid-state Li-O₂ cells in humidified O₂ cycled with cutoff capacities of 100, 150, and 200 mA·hour/$g_{cathode}$. The corresponding energy efficiencies are shown as insets. (**B**) Long-term discharge-charge profiles of cell with 200 mA·hour/$g_{cathode}$ for representative cycle numbers. (**C**) Coulombic and energy efficiencies of the cells with the different cutoff capacities. (**D**) Comparison of cycling performances of solid-state Li-O₂ cell in humidified O₂ and previously reported batteries. Specific capacities of reference cells were recalculated on the basis of the total weight of the cathode (porous electrolyte framework + conductive coating layer). LLTO, lithium lanthanum titanium oxide. (**E**) Discharge/charge profiles of cells with 150 mA·hour/$g_{cathode}$ operated in ambient air with 70 or 55% RH. (**F**) Coulombic and energy efficiencies of the cell operated in air with 70% RH. (**G**) FTIR spectra of cathodes after discharging in humidified O₂ and air with 70% RH. The reference spectra for LiOH·H₂O and Li₂CO₃ are also shown.

200 mA·hour/$g_{cathode}$ for representative cycle numbers are shown in Fig. 5B. As discharging/charging proceeded, the initial capacity of the cell remained stable at 200 mA·hour/$g_{cathode}$ for 665 cycles with a discharge voltage plateau of ~3.1 V, implying that LiOH formation consistently occurred during long-term cycling. The average voltage for charging remained lower than 4.3 V during cycling, indicating that the cathode has outstanding stability and catalytic activity. The x-ray photoelectron spectroscopy analysis of the RBC cathodes before and after cycling also shows that Ru 3d peaks barely changed after long-term cycling, which implies that the oxidation state of Ru(IV) ions almost maintained during the electrochemical cycling (fig. S12). The cells with specific capacities of 100, 150, and 200 mA·hour/$g_{cathode}$ showed excellent cycling performances up to 984, 807, and 665 cycles, respectively (Fig. 5C). Because of the increase in the discharge voltage and stable charging behavior compared to a typical Li_2O_2-based cathode reaction, all cells had high energy efficiencies (average of 75%) during long-term cycling. Note that the stability of the solid electrolyte is a key index for stable long-term cycling performance of the solid-state Li-O_2 cell. The cell failure also could be attributed to the intrinsic instability of the LATP electrolyte layer during electrochemical cycling under humidified and alkaline condition (fig. S13). Further studies are currently underway to develop more stable solid electrolyte to protect LATP under alkaline condition.

Several studies have investigated solid-state Li-O_2 batteries with cathodes composed of an oxide-based solid electrolyte and a conductive carbon material (Fig. 5D). For example, a carbon-coated porous LATP cathode had a capacity of 1000 mA·hour/g for 100 cycles based on the weight of the carbon present (15). However, in terms of the weight of the entire cathode, including both the porous LATP framework and the carbon material, the capacity was only ~41 mA·hour/$g_{cathode}$. Note that the specific capacity of 200 mA·hour/$g_{cathode}$ observed during the cycling tests in this study is based on the total weight of the RBC cathode (table S2). Because the reaction kinetics and cycling stability of the cell improved in the presence of water vapor, this cell could be operated even in ambient air containing moisture. Figure 5E shows the discharge/charge profiles of Li-air cell in air with 70 or 55% relative humidity (RH), which are realistic ranges of average humidity throughout the year. When cycling at a cutoff capacity of 150 mA·hour/$g_{cathode}$, the discharge voltage dropped to ~2.7 V in both cases, which is attributed to the low partial pressure of O_2 (0.21 atm) in air and a low amount of water vapor participating in the discharge reaction (42). The low discharge voltage resulted in the cell operated in air having a lower energy efficiency (~65%) than that in humidified O_2 atmosphere (Fig. 5F). The charge voltage was ~4.2 V in the early stage, while it increased to 4.5 V (cutoff voltage of charging) as the cycling progressed, leading to poor reversibility and Coulombic efficiency of the cell. This may be due to the formation of Li_2CO_3 by CO_2 in air. Figure 5G shows FTIR analysis of cathodes after discharging in humidified O_2 and air with 70% RH compared with reference discharge products in the form of powders. In addition to LiOH formation (fig. S14), the formation of Li_2CO_3 was clearly confirmed by peaks related to C—O stretching vibrations at 1470 and 1410 (v_3, asymmetric), 1085 (v_1), and 860 cm^{-1} (v_2) of carbonate in the cathode discharged in air with 70% RH. In humidified air, LiOH reacted with CO_2 easily, resulting in the formation of Li_2CO_3, which did not decompose readily during charging (43–45). To promote the reversible cathode reaction based on LiOH, it is necessary to limit the

CO_2 content in the air supplied to the cell. However, it is more viable in practice to eliminate and suppress the formation of Li_2CO_3, which should be investigated further to achieve practical Li-air cells with high reversibility that can be used in ambient air.

From a materials perspective, the RBC used here is a model air cathode material for enhancing the reversibility of LiOH-based cathode reactions. As all pores in the RBC cathode can accommodate the discharge product, increasing the cathode porosity would directly increase its capacity (fig. S15). For example, a cathode with a porosity of 80% can deliver a capacity of 1000 mA·hour/g based on the total weight of the cathode. This is at least four times higher than the actual capacity of the conventional cathodes used in Li-ion batteries. Meanwhile, the design of an interlayer between Li metal anode and solid electrolyte layer is another challenging issue to demonstrate the all–solid-state Li-O_2 battery. The all–solid-state Li-O_2 cell using solid polymer electrolyte {polyethylene oxide (PEO) [weight-average molecular weight (M_w) = 600,000], with 1 M LiTF-SI} with a cell configuration of RBC/LATP/PEO/Li was successfully fabricated (fig. S16). Although it showed good discharge/charge behavior and cyclability, the overpotential and long-term stability should be considered further. Related studies on highly porous cathode and sustainable Li metal anode are currently underway with the aim of developing all–solid-state batteries that can deliver more energy.

In summary, we have demonstrated that water vapor additive changes the discharge product from growth-restricted Li_2O_2 to easily grown LiOH for a solid-state Li-O_2 cell, resulting in a notable increase in capacity. The RBC ceramic cathode with only 4 wt % water vapor delivers a specific capacity of 200 mA·hour/g up to 665 cycles, indicating a high reversibility. In addition, the water vapor increased the discharge voltage owing to the formation of LiOH at 3.4 V; in contrast, Li_2O_2 is formed at 2.96 V in the absence of the additive. The proposed strategy of water vapor additive is inexpensive and simple and thus can be easily applied to the most of solid-state Li-O_2 cells, which require the high capacity, high efficiency, and high energy density. This can further make the solid-state Li-O_2 technology more competitive in the battery market.

MATERIALS AND METHODS
Synthesis of RBC material
The RuO_2 (99.9%), La_2O_3 (99.99%), and Li_2CO_3 (99.9%) reagents were obtained commercially (Sigma-Aldrich, Merck) and used as received. The reagents were ball milled in a zirconia jar with ethanol in a target volume ratio of RuO_2:La_2LiRuO_6 = 2:3. The powder mixture was then calcined at 800°C for 4 hours in air. Then, the calcined powder was ground and pressed into pellets with a diameter of 13 mm and a thickness of approximately l mm. These pellets were fired at 1200°C for 24 hours in air and cooled to room temperature. To prepare the RBC cathode thin film, the pellets were again ball milled using a planetary mill to reduce the particle size distribution.

Material characterization
The crystal structures of the synthesized RBC and cycled electrodes were characterized using XRD (Bruker D8 ADVANCE; Cu Kα radiation, λ = 1.5406 Å) at a scan rate of 6°/min over a 2θ range of 10° to 90°. Ru K-edge XAS and O K-edge XAS were performed at beamlines 7-BM and 7-ID-1, respectively, of the National Synchrotron Light Source II in Brookhaven National Laboratory. Elemental

maps for Ru and La atoms in RBC cathode were obtained using HAADF-STEM (FEI Tecnai Osiris) at a 200-kV acceleration voltage. The FTIR spectra of discharged cathodes and reference powders were obtained using an FTIR microscope (Hyperion 3000, Bruker). For the morphological analyses of the RBC cathode and discharge products, a field-emission SEM system (Nova NanoSEM, FEI) was used.

Conductivity measurements

The Li-ion conductivity of the RBC at room temperature was determined by the dc polarization of an electron-blocking cell at 20°C. A porous separator (Celgard 3501) for absorbing the electrolyte (1 M LiTFSI in PC) was attached on each side of the RBC pellet (with a diameter of 13 mm and a thickness of 1 mm). In addition, a piece of Li metal foil was attached to each side. A constant potential of 100 mV was applied to the electron-blocking cell for 1800 s until the current became independent of time. The total Li-ion conductivity was calculated, while the cell was in the steady state. In addition, the electronic conductivity of the RBC at 20°C was determined from the current-voltage curve of an ion-blocking cell with Au electrodes.

Li-O$_2$ cell tests

A freestanding cathode film was fabricated by the bar-coating process using a dispersion composed of the RBC powder and a binder (Butvar B-79, Eastman) in a weight ratio of 2:1 in ethanol. RBC cathodes with mass loading rates of 0.2 to 0.5 mg were used for the electrochemical analysis and long-term cycling test. A dried cathode film was punched to the desired size and attached to an LATP plate. This was followed by calcination at 400°C to remove the polymeric binder. A pouch-type Li metal anode was fabricated to protect the Li metal from moisture during operation in the humidified atmosphere. The cathode/LATP plate, the electrolyte (1 M LiTFSI in PC) with a polymer separator as an interlayer, and a piece of Li metal foil (175 μm; Honjo) were vacuum-sealed using thermoplastic sealing film (Meltonix 1170-25, Solaronix) while leaving a 16-mm-diameter window. The thus assembled Li-O$_2$ cell was operated in a stainless steel chamber with a vial containing a small amount of water at 40°C; before this step, purging was performed using pure O$_2$. This ensured that the atmosphere contained 4 wt % water vapor, as calculated by dividing the saturated water vapor content by the total amount of water vapor and O$_2$ in the chamber at 40°C. The CV measurements were performed using a potentiostat (VMP3, Bio-Logic Science Instruments) for voltages of 2.2 to 4.5 V (versus Li/Li$^+$) at a scan rate of 0.5 mV/s in dry and humidified O$_2$. The galvanostatic discharge-charge tests were conducted using a battery test system (TOSCAT, TOYO SYSTEM) for the same voltage range at different current densities in either humidified O$_2$ (100% RH at 40°C) or ambient air (70 or 55% RH at 40°C).

First-principles calculations

First-principles calculations were performed with the Perdew-Burke-Ernzerhof exchange-correlation functional using the spin-polarized generalized gradient approximation (GGA) functional (46). The projector-augmented wave pseudo-potentials were used as implemented in the Vienna Ab initio Simulation Package (47). A Hubbard-type U parameter (GGA + U) (48) was added to correct the on-site Coulomb interactions, with U[Ru] = 4.0 eV (49) and U[La] = 7.5 eV (50).

SUPPLEMENTARY MATERIALS

Supplementary material for this article is available at https://science.org/doi/10.1126/sciadv.abm8584

REFERENCES AND NOTES

1. K. M. Abraham, Z. Jiang, A polymer electrolyte-based rechargeable lithium/oxygen battery. *J. Electrochem. Soc.* **143**, 1–5 (1996).
2. T. Ogasawara, A. Débart, M. Holzapfel, P. Novák, P. G. Bruce, Rechargeable Li$_2$O$_2$ electrode for lithium batteries. *J. Am. Chem. Soc.* **128**, 1390–1393 (2006).
3. G. Girishkumar, B. McCloskey, A. C. Luntz, S. Swanson, W. Wilcke, Lithium–air battery: Promise and challenges. *J. Phys. Chem. Lett.* **1**, 2193–2203 (2010).
4. N. Imanishi, O. Yamamoto, Rechargeable lithium–air batteries: Characteristics and prospects. *Mater. Today* **17**, 24–30 (2014).
5. X.-X. Wang, D.-H. Guan, F. Li, M.-L. Li, L.-J. Zheng, J.-J. Xu, Magnetic and optical field multi-assisted Li–O$_2$ batteries with ultrahigh energy efficiency and cycle stability. *Adv. Mater.* **34**, 2104792–2104801 (2021).
6. M. Li, X. Wang, F. Li, L. Zheng, J. Xu, J. Yu, A bifunctional photo-assisted Li–O$_2$ battery based on a hierarchical heterostructured cathode. *Adv. Mater.* **32**, 1907098–1907107 (2020).
7. D. Sharon, V. Etacheri, A. Garsuch, M. Afri, A. A. Frimer, D. Aurbach, On the challenge of electrolyte solutions for Li–air batteries: Monitoring oxygen reduction and related reactions in polyether solutions by spectroscopy and EQCM. *J. Phys. Chem. Lett.* **4**, 127–131 (2013).
8. B. D. McCloskey, A. Speidel, R. Scheffler, D. C. Miller, V. Viswanathan, J. S. Hummelshøj, J. K. Nørskov, A. C. Luntz, Twin problems of interfacial carbonate formation in nonaqueous Li–O$_2$ batteries. *J. Phys. Chem. Lett.* **3**, 997–1001 (2012).
9. M. M. Ottakam Thotiyl, S. A. Freunberger, Z. Peng, P. G. Bruce, The carbon electrode in nonaqueous Li–O$_2$ cells. *J. Am. Chem. Soc.* **135**, 494–500 (2012).
10. S. A. Freunberger, Y. Chen, Z. Peng, J. M. Griffin, L. J. Hardwick, F. Bardé, P. Novák, P. G. Bruce, Reactions in the rechargeable lithium–O$_2$ battery with alkyl carbonate electrolytes. *J. Am. Chem. Soc.* **133**, 8040–8047 (2011).
11. B. D. McCloskey, D. S. Bethune, R. M. Shelby, G. Girishkumar, A. C. Luntz, Solvents' critical role in nonaqueous lithium–oxygen battery electrochemistry. *J. Phys. Chem. Lett.* **2**, 1161–1166 (2011).
12. H. Wang, X. Wang, M. Li, L. Zheng, D. Guan, X. Huang, J. Xu, J. Yu, Porous materials applied in nonaqueous Li–O$_2$ batteries: Status and perspectives. *Adv. Mater.* **32**, 2002559–2002579 (2020).
13. L.-N. Song, W. Zhang, Y. Wang, X. Ge, L.-C. Zou, H.-F. Wang, X.-X. Wang, Q.-C. Liu, F. Li, J.-J. Xu, Tuning lithium-peroxide formation and decomposition routes with single-atom catalysts for lithium–oxygen batteries. *Nat. Commun.* **11**, 2191–2201 (2020).
14. N. Luo, G.-J. Ji, H.-F. Wang, F. Li, Q.-C. Liu, J.-J. Xu, Process for a free-standing and stable all-metal structure for symmetrical lithium–oxygen batteries. *ACS Nano* **14**, 3281–3289 (2020).
15. X. B. Zhu, T. S. Zhao, Z. H. Wei, P. Tan, G. Zhao, A novel solid-state Li–O$_2$ battery with an integrated electrolyte and cathode structure. *Energ. Environ. Sci.* **8**, 2782–2790 (2015).
16. Y. Liu, B. Li, H. Kitaura, X. Zhang, M. Han, P. He, H. Zhou, Fabrication and performance of all-solid-state Li–air battery with SWCNTs/LAGP cathode. *ACS Appl. Mater. Interfaces* **7**, 17307–17310 (2015).
17. H. T. T. Le, D. T. Ngo, P. N. Didwal, J. G. Fisher, C.-N. Park, I.-D. Kim, C.-J. Park, Highly efficient and stable solid-state Li–O$_2$ batteries using a perovskite solid electrolyte. *J. Mater. Chem. A* **7**, 3150–3160 (2019).
18. X. Chi, M. Li, J. Di, P. Bai, L. Song, X. Wang, F. Li, S. Liang, J. Xu, J. Yu, A highly stable and flexible zeolite electrolyte solid-state Li–air battery. *Nature* **592**, 551–557 (2021).
19. M. D. Radin, D. J. Siegel, Charge transport in lithium peroxide: Relevance for rechargeable metal–air batteries. *Energ. Environ. Sci.* **6**, 2370–2379 (2013).
20. V. Viswanathan, K. S. Thygesen, J. S. Hummelshøj, J. K. Nørskov, G. Girishkumar, B. D. McCloskey, A. C. Luntz, Electrical conductivity in Li$_2$O$_2$ and its role in determining capacity limitations in non-aqueous Li–O$_2$ batteries. *J. Chem. Phys.* **135**, 214704–214713 (2011).
21. F. Li, S. Wu, D. Li, T. Zhang, P. He, A. Yamada, H. Zhou, The water catalysis at oxygen cathodes of lithium–oxygen cells. *Nat. Commun.* **6**, 7843–7849 (2015).
22. S. Wu, J. Tang, F. Li, X. Liu, H. Zhou, Low charge overpotentials in lithium–oxygen batteries based on tetraglyme electrolytes with a limited amount of water. *Chem. Commun.* **51**, 16860–16863 (2015).
23. Y. G. Zhu, Q. Liu, Y. Rong, H. Chen, J. Yang, C. Jia, L.-J. Yu, A. Karton, Y. Ren, X. Xu, S. Adams, Q. Wang, Proton enhanced dynamic battery chemistry for aprotic lithium–oxygen batteries. *Nat. Commun.* **8**, 14308–14315 (2017).
24. T. Liu, Z. Liu, G. Kim, J. T. Frith, N. Garcia-Araez, C. P. Grey, Understanding LiOH chemistry in a ruthenium-catalyzed Li–O$_2$ battery. *Angew. Chemie Int. Ed.* **56**, 16057–16062 (2017).
25. P. Tan, W. Shyy, T. S. Zhao, R. H. Zhang, X. B. Zhu, Effects of moist air on the cycling performance of non-aqueous lithium-air batteries. *Appl. Energy* **182**, 569–575 (2016).
26. Y. Suzuki, K. Watanabe, S. Sakuma, N. Imanishi, Electrochemical performance of an all-solid-state lithium-oxygen battery under humidified oxygen. *Solid State Ion.* **289**, 72–76 (2016).

27. J. Lu, S. Dey, I. Temprano, Y. Jin, C. Xu, Y. Shao, C. P. Grey, Co$_3$O$_4$-catalyzed LiOH chemistry in Li–O$_2$ batteries. *ACS Energy Lett.* **5**, 3681–3691 (2020).

28. X. Bi, M. Li, C. Liu, Y. Yuan, H. Wang, B. Key, R. Wang, R. Shahbazian-Yassar, L. A. Curtiss, J. Lu, K. Amine, Cation additive enabled rechargeable LiOH-based lithium–oxygen batteries. *Angew. Chem. Int. Ed.* **59**, 22978–22982 (2020).

29. Y. Lee, J. Suntivich, K. J. May, E. E. Perry, Y. Shao-Horn, Synthesis and activities of rutile IrO$_2$ and RuO$_2$ nanoparticles for oxygen evolution in acid and alkaline solutions. *J. Phys. Chem. Lett.* **3**, 399–404 (2012).

30. L. F. Mattheiss, Electronic structure of RuO$_2$, OsO$_2$, and IrO$_2$. *Phys. Rev. B* **13**, 2433–2450 (1976).

31. W. Sugimoto, H. Iwata, K. Yokoshima, Y. Murakami, Y. Takasu, Proton and electron conductivity in hydrous ruthenium oxides evaluated by electrochemical impedance spectroscopy: The origin of large capacitance. *J. Phys. Chem. B* **109**, 7330–7338 (2005).

32. Z.-F. Huang, J. Wang, Y. Peng, C.-Y. Jung, A. Fisher, X. Wang, Design of efficient bifunctional oxygen reduction/evolution electrocatalyst: Recent advances and perspectives. *Adv. Energ. Mater.* **7**, 1700544–1700564 (2017).

33. A. B. Santibáñez-Mendieta, C. Didier, K. K. Inglis, A. J. Corkett, M. J. Pitcher, M. Zanella, J. F. Shin, L. M. Daniels, A. Rakhmatullin, M. Li, M. S. Dyer, J. B. Claridge, F. Blanc, M. J. Rosseinsky, La$_3$Li$_3$W$_2$O$_{12}$: Ionic diffusion in a perovskite with lithium on both A- and B-sites. *Chem. Mater.* **28**, 7833–7851 (2016).

34. A. Grimaud, A. Demortière, M. Saubanère, W. Dachraoui, M. Duchamp, M.-L. Doublet, J.-M. Tarascon, Activation of surface oxygen sites on an iridium-based model catalyst for the oxygen evolution reaction. *Nat. Energy* **2**, 16189–16198 (2017).

35. J. Haines, J. M. Léger, O. Schulte, S. Hull, Neutron diffraction study of the ambient-pressure, rutile-type and the high-pressure, CaCl$_2$-type phases of ruthenium dioxide. *Acta Crystallogr. Sect. B Struct. Sci.* **53**, 880–884 (1997).

36. P. D. Battle, C. P. Grey, M. Hervieu, C. Martin, C. A. Moore, Y. Paik, Structural chemistry and magnetic properties of La$_2$LiRuO$_6$. *J. Solid State Chem.* **175**, 20–26 (2003).

37. S. Riegg, A. Reller, A. Loidl, S. G. Ebbinghaus, Valence properties of Cu and Ru in titanium-substituted LnCu$_3$Ru$_4$O$_{12+\delta}$ (Ln = La, Pr, Nd) investigated by XANES and TGA. *Dalt. Trans.* **44**, 10852–10859 (2015).

38. R. Amin, Y.-M. Chiang, Characterization of electronic and ionic transport in Li$_{1-x}$Ni$_{0.33}$Mn$_{0.33}$Co$_{0.33}$O$_2$ (NMC333) and Li$_{1-x}$Ni$_{0.50}$Mn$_{0.20}$Co$_{0.30}$O$_2$ (NMC523) as a function of Li content. *J. Electrochem. Soc.* **163**, A1512–A1517 (2016).

39. S. B. Ma, H. J. Kwon, M. Kim, S.-M. Bak, H. Lee, S. N. Ehrlich, J.-J. Cho, D. Im, D.-H. Seo, Mixed ionic–electronic conductor of perovskite Li$_x$La$_y$MO$_{3-\delta}$ toward carbon-free cathode for reversible lithium–air batteries. *Adv. Energy Mater.* **10**, 2001767 (2020).

40. Z. Lyu, Y. Zhou, W. Dai, X. Cui, M. Lai, L. Wang, F. Huo, W. Huang, Z. Hu, W. Chen, Recent advances in understanding of the mechanism and control of Li$_2$O$_2$ formation in aprotic Li–O$_2$ batteries. *Chem. Soc. Rev.* **46**, 6046–6072 (2017).

41. J. D. Rodriguez-Blanco, S. Shaw, L. G. Benning, The kinetics and mechanisms of amorphous calcium carbonate (ACC) crystallization to calcite, via vaterite. *Nanoscale* **3**, 265–271 (2011).

42. H. Kwon, H.-C. Lee, J. Ko, I. Jung, H.-C. Lee, H. Lee, M. Kim, D.-J. Lee, H.-J. Kim, T.-Y. Kim, D. Im, Effects of oxygen partial pressure on Li-air battery performance. *J. Power Sources* **364**, 280–287 (2017).

43. T. Zhang, H. Zhou, A reversible long-life lithium–air battery in ambient air. *Nat. Commun.* **4**, 1817 (2013).

44. H.-K. Lim, H.-D. Lim, K.-Y. Park, D.-H. Seo, H. Gwon, J. Hong, W. A. Goddard, H. Kim, K. Kang, Toward a lithium–"air" battery: The effect of CO$_2$ on the chemistry of a lithium–oxygen cell. *J. Am. Chem. Soc.* **135**, 9733–9742 (2013).

45. M. Asadi, B. Sayahpour, P. Abbasi, A. T. Ngo, K. Karis, J. R. Jokisaari, C. Liu, B. Narayanan, M. Gerard, P. Yasaei, X. Hu, A. Mukherjee, K. C. Lau, R. S. Assary, F. Khalili-Araghi, R. F. Klie, L. A. Curtiss, A. Salehi-Khojin, A lithium-oxygen battery with a long cycle life in an air-like atmosphere. *Nature* **555**, 502–506 (2018).

46. J. P. Perdew, K. Burke, M. Ernzerhof, Generalized gradient approximation made simple. *Phys. Rev. Lett.* **77**, 3865–3868 (1996).

47. G. Kresse, J. Furthmüller, Efficient iterative schemes for *ab initio* total-energy calculations using a plane-wave basis set. *Phys. Rev. B* **54**, 11169–11186 (1996).

48. S. L. Dudarev, G. A. Botton, S. Y. Savrasov, C. J. Humphreys, A. P. Sutton, Electron-energy-loss spectra and the structural stability of nickel oxide: An LSDA+U study. *Phys. Rev. B* **57**, 1505–1509 (1998).

49. M. Sathiya, A. M. Abakumov, D. Foix, G. Rousse, K. Ramesha, M. Saubanère, M. L. Doublet, H. Vezin, C. P. Laisa, A. S. Prakash, D. Gonbeau, G. VanTendeloo, J.-M. Tarascon, Origin of voltage decay in high-capacity layered oxide electrodes. *Nat. Mater.* **14**, 230–238 (2015).

50. D. Qian, B. Xu, H.-M. Cho, T. Hatsukade, K. J. Carroll, Y. S. Meng, Lithium lanthanum titanium oxides: A fast ionic conductive coating for lithium-ion battery cathodes. *Chem. Mater.* **24**, 2744–2751 (2012).

$Science$Advances

Carbon-free high-performance cathode for solid-state Li-O$_2$ battery

Mokwon KimHyunpyo LeeHyuk Jae KwonSeong-Min BakCherno JayeDaniel A. FischerGabin YoonJung O. ParkDong-Hwa SeoSang Bok MaDongmin Im

View the article online
https://www.science.org/doi/10.1126/sciadv.abm8584
Permissions
https://www.science.org/help/reprints-and-permissions

Use of this article is subject to the Terms of service